Coherent-to-semi-coherent transition of precipitates in niobium-hydrogen thin films

Kai Nörthemann
Institut für Materialphysik, University of Göttingen, Friedrich-Hund-Platz 1, 37077 Göttingen, Germany

Astrid Pundt*
Insitut für Materialphysik, University of Göttingen, Friedrich-Hund-Platz 1, 37077 Göttingen, Germany
(Received 9 July 2007; revised manuscript received 5 May 2008; published 11 July 2008)

Nucleation and growth in thin films are studied by using niobium-hydrogen (Nb-H) as model system. Hydride precipitation in thin films results in local surface topography changes that can be monitored by scanning tunneling microscopy. The local film expansion can be used to detect hydride precipitates, to study their growth, to gain information about their shape and their lattice coherency. With the help of theoretical calculations, it will be shown that cylindrical Nb-H precipitates evolve in early stages. These precipitates are coherent to the matrix as long as the film is thin and the hydride size is below a critical volume. Above this critical volume, a coherent-to-semi-coherent transition occurs. The critical size is controlled by the balance between the elastic energy stored in the coherent precipitate and the energy needed for the formation of dislocations. Consequently, films below 26 nm thickness keep coherency for all hydride precipitate volumes and never get semi-coherent.

DOI: 10.1103/PhysRevB.78.014105 PACS number(s): 81.30.Mh, 68.55.Nq, 68.37.Ef, 47.11.Fg

I. INTRODUCTION

Precipitation and growth in bulk alloys have been an important topic of research for many decades.[1–4] Models that describe homogeneous precipitation and growth were developed and have been successfully applied.[3,5] Additionally, misfitting particles in matrices were analyzed, both incoherently and coherently matched to the embedding matrix.[6–8] Here, the formation of dislocations is one topic of interest. Early stages of homogeneous precipitation and the impact of stress are issues addressed nowadays.[9–13] When thin films are examined, heterogeneous defects like surfaces, interfaces and grain boundaries influence phase transformations so that theories requiring homogeneous conditions can barely be applied. Heterogeneous precipitation and growth will most probably dominate.

Phase transitions in thin films are expected to differ from that in bulk because of mechanical stress and the reduced dimensionality of the system.[14–17] Studies of different research groups focus on the thermodynamics of polycrystalline and epitaxial metal-hydrogen (M-H) thin films; they mostly collect temperature dependent pressure-concentration isotherms or pressure-lattice-parameter isotherms. Film thickness dependent isotherms were reported for niobium-hydrogen (Nb-H) and controversially discussed by different authors.[15,16,18]

For thin films like Holmium-H, Yttrium-H and Gadolinium-H, hydride formation was monitored by scanning tunneling microscopy (STM) verifying the large vertical film expansion upon hydride formation.[19–22]

Surface topography was intensively studied, mainly the later stages between the di-and trihydride, during loading and unloading. While Pundt *et al.* mainly focus on mechanical stress, plastic deformation and lattice expansion of thin films, Kerssemakers *et al.* discuss a twinning mechanism to explain the surface topography.[16,21,23] However, the study of early stages of precipitation in thin M-H films was not performed in any of these works. Therefore, we focus on this field. We use Nb-H as model system.[24–26] In M-H alloys, the hydrogen content in the film can be increased by increasing the outside hydrogen gas pressure.[16,27] Because H solves interstitially in the host lattice and tunneling assists its diffusion, alloying can be performed at room temperature in short periods of time. Precipitates are easy to detect since a large lattice expansion accompanies the phase transformation in Nb-H, where $\Delta a/a_0 = 0.058\, c_H$ in bulk alloys when H concentration c_H is given in H/Nb.[24–26] For bulk Nb-H, phase transition between the solid solution α-phase and the high-concentration hydride phase ($c_H = 72\%$),[28] occurs at a hydrogen gas pressure of 2.3×10^{-5} Pa.[29]

For clamped thin films, the lattice expansion occurs mainly unidirectional and is much larger.[15,30–32] The strong out-of-plane expansion upon hydride formation can be used to study hydride precipitation and growth by surface topography studies.[33] By using the hydrogen-related lattice expansion it is possible to distinguish α-phase regions from the hydride-phase regions by monitoring the film surface topography. However, it cannot simply be judged in what depth the hydride exists, if it does not cover the thickness of the complete film. Additional assumptions have to be made here.

In this study surface topography changes during phase transformation in thin Nb-H films are examined. We will show that information about the hydride morphology inside the film can be gained by comparing experimental results on the film surface with theoretical calculations on hydride precipitates inside the films. In detail, a coherent-to-semi-coherent transition can be directly monitored.

II. EXPERIMENT AND RESULTS

A. Sample preparation

Epitaxial films were used to exclude as many microstructural contributions as possible.[16] Such Nb films were grown on $(11\bar{2}0)$ sapphire substrates with a miscut of less than 0.1°

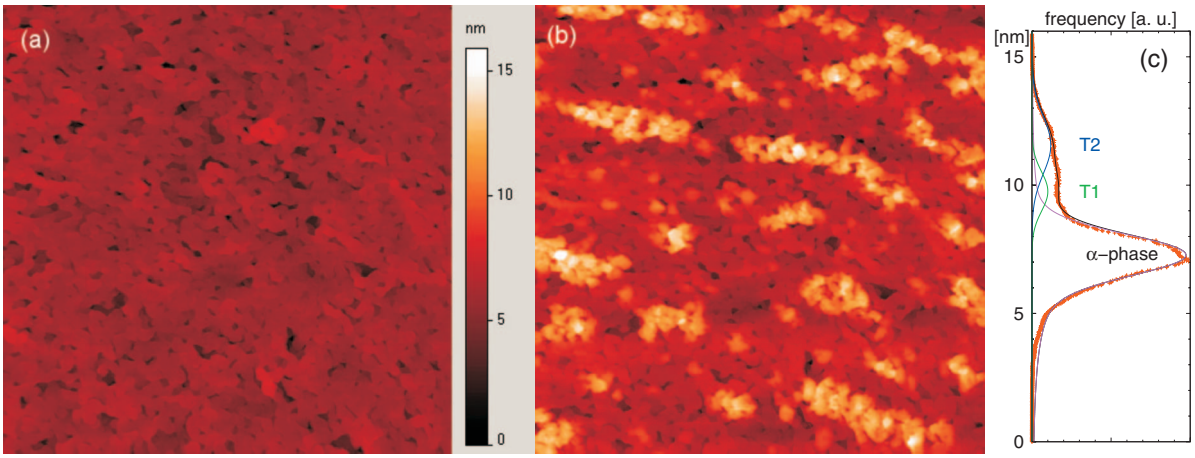

FIG. 1. (Color) Topographical STM images of an 80 nm niobium-hydrogen film (image size 2.5×2.5 μm). In (a) the film surface is shown at a hydrogen gas pressure of 2×10^{-7} Pa. In (b) the film surface shows surface topography changes after 67 h of hydrogen gas exposure at 9×10^{-5} Pa. The locally elevated regions are visible. The related histogram of the height (c) reflects a bimodal distribution of these elevations which split up (marked with T1 and T2). The large peak (marked with α-phase) gives the base level. For clarity the same z range is chosen in the STM images.

or 0.2°, on which Nb films grow with an orientation relationship, i.e., $[1\bar{1}1]_{Nb}\|[0001]_{Al_2O_3}$ and $[1\bar{1}\bar{2}]_{Nb}\|[1\bar{1}00]_{Al_2O_3}$.[34–37] The films were prepared by Ar sputtering (sputter rate: 0.6 nm/min) in an UHV system with a base pressure less than 3×10^{-8} Pa which increases at the deposition temperature of 800 °C to about 1×10^{-5} Pa. For the sputtering process an argon pressure of 8×10^{-3} Pa was applied. Films with thicknesses between 40 and 120 nm were prepared. The surfaces of these epitaxial niobium films contain terraces with atomic steps height and with a diameter of approx 80 nm. To facilitate hydrogen absorption at room temperature, a Pd catalyst of about one monolayer is used.[33] This palladium was deposited after the sample cooled down to room temperature. It forms small islands with a diameter of 7 ± 2 nm; their height is about two monolayers. After preparation, the films are transferred to the STM chamber without breaking the UHV conditions. Therefore, no cap layer is needed to protect the Nb film from oxidation.

B. Hydrogen loading

Scanning tunneling microscopy can be performed during hydrogen loading from the gas phase with constant pressures between 10^{-7} and 10^{-2} Pa.[33] Hydrogen gas with a nominal purity of 5.6N is used. Whereas for bulk material Sieverts law relates the concentration c_H with the equilibrium gas pressure p ($c_H=S\sqrt{p_{H_2}}$), this relation is not simply applicable to thin films.[16]

The hydrogen concentration in thin films is increased by increasing the outside hydrogen gas pressure, but the internal concentration is *a priori* unknown. Further experiments like concentration dependent x-ray diffraction, film resistivity measurements, electromotoric force measurements or the N15-method have to be performed to link pressure and concentration.[18,31,32,38–41] All STM measurements were performed at room temperature, with a Micro STM from Omicron, where mechanically thinned Pt/Ir tips are used, with $I_{gap}=1$ nA, $U_{gap}=0.5$ V.

C. Hydride precipitates in Nb films

The film surface topography was studied while hydrogen gas pressure was increased stepwise. The phase transition pressure of 6×10^{-5} Pa was found to be rather independent of the film thickness. This phase transition pressure is in good accordance with that for bulk Nb-H (2.3×10^{-5} Pa).[29] At pressures above this value hydride formation becomes detectable at the film surface.[16,42] Figure 1 shows two topographical STM images of an 80-nm-thin Nb-H film obtained at different hydrogen gas pressures. Figure 1(a) (2×10^{-7} Pa) shows a film surface which does not differ from the virgin surface without hydrogen exposure. The Nb-H system film is still in the α-phase at this hydrogen gas pressure. Figure 1(b) was taken after 67 h of hydrogen exposure at a pressure of 9×10^{-5} Pa. This exposure leads to significant surface topography changes. Since the pressure slightly exceeds the phase transformation pressure, the surface topography changes are induced by partial hydride formation in the Nb-H film. In this figure, the base level of a large surface fraction does not differ significantly from that measured before hydrogen exposure. These regions consist of the remaining α-phase in the Nb-H film. Other regions are elevated, which is shown in bright colors. According to the strong out-of-plane expansion of the hydride phase compared to the α-phase, hydride is expected in regions elevated with respect to α-phase base level of Fig. 1(b). Thus, α-phase-related regions and hydride-phase-related regions are distinguished by the local topography.

In Fig. 1(b) two different types of hydride-related topographies are visible: small hillocks with round shape and a limited lateral size, T1, and large elongated topographies, T2. In the 80 nm film the height difference between base level and the top of the small T1 hillocks amounts to only 2.1 ± 0.3 nm. The corresponding radii vary. But, there is no hillock with a radius larger than 35 ± 2 nm. The height difference between base level and the T2 topographies is much larger: For the 80 nm film it is about $\Delta z=4.9\pm0.5$ nm. This

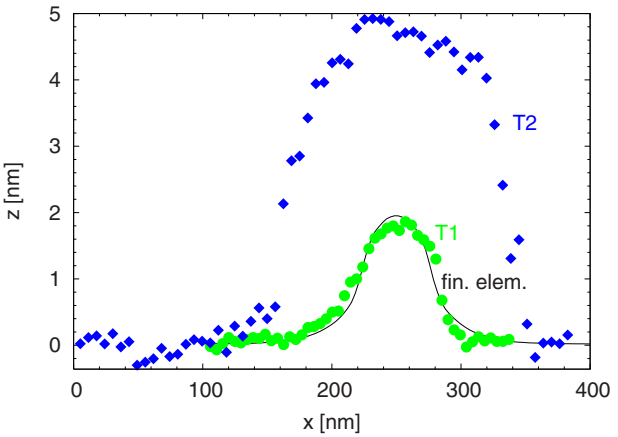

FIG. 2. (Color online) Typical line profiles of T1 and T2 topographies, as measured on a 70 nm Nb-H film. T2 topographies are significantly larger than T1 topographies ("hillocks"). Also, the height profile rises steeper for T2 topographies and their surface is comparably rough. This graph also includes a calculated finite element method profile. It matches the T1 topography.

can be seen in the histogram of heights which is shown in Fig. 1(c). It divides into three different Gaussian curves: one for the α-phase, one for the T1 hillocks, and one for the T2 topographies.

The line profiles of T1 and T2 topographies differ strongly. This is shown in Fig. 2 for a 70 nm Nb-H film. Beside their different heights, the surface of the T2 topographies is rougher than that of the T1 topography and that of the α-phase base level. In the line profile of the T2 topography several individual steps of about 0.2 nm are visible. This stepped roughness on the T2 topographies can be even more pronounced. This is shown in Fig. 3 which exclusively monitors the surface of a large T2 topography. The spatial arrangement of these steps is a linear chain, preferentially laying in the film's $\langle \bar{1}11 \rangle$ and $\langle \bar{1}13 \rangle$ directions. These directions are expected to occur when (011) and $(1\bar{2}1)$ glide planes cut

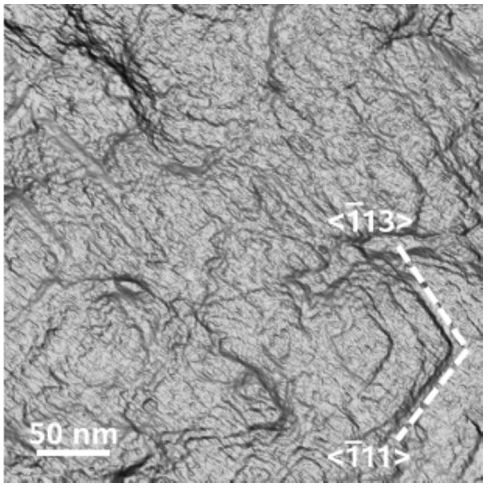

FIG. 3. STM-surface image of a large T2 topography on a 100 nm Nb-H film. The surface roughness consists of linear glide step predominately laying in $\langle \bar{1}11 \rangle$ and $\langle \bar{1}13 \rangle$ lattice directions.

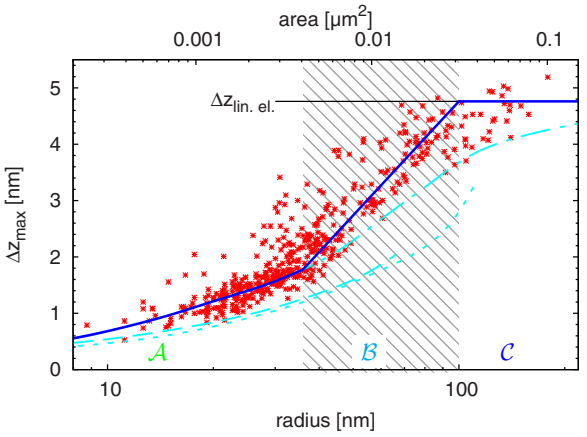

FIG. 4. (Color online) Experimental heights Δz_{max} and related radii of topographies formed upon hydrogen loading of a 70-nm-thin niobium film (data points). The hydrogen gas pressure was 1×10^{-4} Pa H_2. A direct correlation is found which is marked by a straight line to guide the eye. A strong height increase occurs above a critical radius of $r_{crit}=36\pm3$ nm. A saturation at a maximum height of $\Delta z_{max}=4.8$ nm is found for radii above $r_{crit}=100$ nm. Also implemented are finite element method calculation results (cylinder: — ·; sphere: – –; ellipsoid: ···).

the (110) film surface plane (for further details, see Ref. 33). Thus, surface roughening consists of individual surface glide steps. The rim of T2 topographies is steeper than that of T1 topographies. Rims of T1 topographies increase with a slope of 3° with respect to the base level while those of T2 topographies usually exceed 10°. We like to advert to the different axes scales in Fig. 2. The different slopes mainly relate to the different total height of the two topographies.

Figure 4 shows the height Δz of T1 and T2 topographies depending on the lateral size (area and equivalent radius are used as axes) as deduced from five subsequently taken STM images of a 70-nm-thin Nb-H film. A strong correlation between height and size can be observed (marked by a straight line to guide the eye): while for small topographies with radii below 36 ± 3 nm ($\mathcal{A}$) the height Δz is rather small, it strongly increases above radii of 36 ± 3 nm (hatched region $\mathcal{B}$). At an area of ≈ 0.03 μm^2 (equivalent to a radius of ≈ 100 nm, marked with $\mathcal{C}$), the measured expansion of the topographies reaches a saturation value which is equivalent to the value obtained by using linear elastic theory, $\Delta z_{lin.el.}=4.8$ nm. This is marked with a horizontal solid line in Fig. 4. In this graph, more theoretical curves are included which result from the finite element method (FEM) calculations described in the discussion.

T1 and T2 topographies evolve differently for films with different film thicknesses. This is summarized in Fig. 5 which shows the experimentally determined dependencies of the height Δz of T1 (a) and T2 (b) and the maximum lateral radius r_{crit} of T1 for different film thicknesses (40 nm, 50 nm, 70 nm, 80 nm, 100 nm, and 120 nm).

For T1 [Fig. 5(a)], Δz shows no film thickness dependency and is about 1.9 ± 0.1 nm. But the maximum observed lateral radius r_{crit} of T1 topographies slightly decreases with increasing film thickness, starting from 40 ± 2 nm for a 40 nm film to 35 ± 2 nm for an 80 nm film.

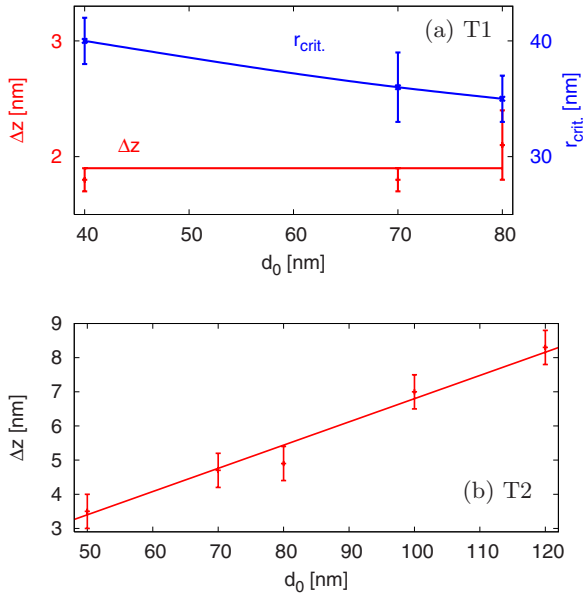

FIG. 5. (Color online) Height Δz (and lateral radius r_{crit}) of T1 and T2 topographies, (a) and (b), as function of the film thickness. (a) For T1 topographies, the height Δz is independent of the film thickness. The maximum size r_{crit} decreases with increasing film thickness. For T2 topographies, (b) shows a linear dependency of the height $\Delta z = 6.8 \pm 0.1\% \times d_0$ from the film thickness d_0.

For the T2 topographies, Fig. 5(b), a linear dependency holds between height change Δz and film thickness d_0, $\Delta z = 6.8 \pm 0.1\% \times d_0$. This is displayed in Fig. 5(b). No maximum lateral size was found for T2 topographies. They just grow and cover the complete image. Thus, no r_{crit} is plotted for T2 topographies. But, the film thickness dependency of T2 topographies is just valid for thicker films. For a 20 nm Nb-H film, T2 topographies were not experimentally observed.

Further, T2 topographies are not reversible. Reducing the hydrogen pressure below 1×10^{-6} Pa does not change the surface topography even though this pressure is far below the unloading transition pressure. At the same pressure, T1 topographies were not observed anymore.

III. DISCUSSION

For Nb-H thin films strong surface topography changes are detectable above a pressure of 6×10^{-5} Pa. This pressure was found to be rather independent of the film thickness. It is in good accordance with the phase transition pressure of 2.3×10^{-5} Pa for bulk Nb-H.[29] The experimental results suggest a direct link between hydride formation in the Nb-H films and the observed surface topographies.[16,42] The surface topography changes occur in spatially localized regions. Other regions remain with their original topography. Thus, hydride-phase-related regions and α-phase-related regions can be well distinguished by the local topography.

The height of the T2-surface topographies, as summarized in Fig. 5(b), can be explained with regard to the out-of-plane lattice expansion during hydride formation. Calculations using the theory of linear elasticity for a Nb film clamped to a rigid substrate give an expansion of $\Delta a/a_0 = 0.136\, c_H$ [H/Nb].[15,30–32] Earlier XRD-measurements have confirmed the linear increase with H concentration as long as the sample stays in the linear elastic regime.[32] For larger H concentrations the expansion is reduced, but is mostly larger than that of the bulk system. For the sake of completeness it should be stated that during H uptake compressive stress evolves laterally in thin films, and it can reach several GPa. For Nb-H thin films maximum stresses of −3.4 GPa have been measured accompanied with an initial stress increase of about −9.6 GPa/c_H.[32] The initial stress increase, also, is in good accordance with calculations using the theory of linear elasticity on a film that is clamped to a rigid substrate.

Upon hydride formation in a thin film with a thickness d_0, a maximum height change in the topography of

$$\Delta d = d_0\, 0.136\, \Delta c_H = d_0\, 0.068 \qquad (1)$$

is expected,[24,31,32,43] when a mean concentration difference of $\Delta c_H = 0.5$ H/Nb between α-phase and hydride phase is assumed. For a 40 nm film local hydride-related surface topography changes of 2.7 nm are expected.

The concentration difference Δc_H of the miscibility gap is one point to be addressed shortly. Phase boundary concentrations in thin metal-hydrogen films are reported to differ from bulk values and are influenced by microstructure, film thickness, and mechanical stress.[16] For epitaxial Nb-H films below 100 nm, Dornheim determined a mean α-hydride miscibility gap of $\Delta c_H \approx 0.5$ H/Nb[43] compared to $\Delta c_H = 0.66$ H/Nb for bulk Nb-H.[24] However, Laudahn and Dornheim also reported a slight thickness dependency:[16,43] For $d_0 = 190$ nm Laudahn reports $\Delta c_H = 0.64$ H/Nb which Dornheim found to decrease with the film thickness. For 100 nm a $\Delta c_H = 0.54 - 0.64$ H/Nb was determined while for 35 nm $\Delta c_H = 0.38 - 0.43$ H/Nb. This slight thickness dependency is neglected in this work.

A good agreement between T2 topographies and the linear elastic theory results can be seen in Fig. 5(b) where the theoretical line with a slope of $6.8 \pm 0.1\%$ calculated by using Eq. (1) directly matches the experimental $\Delta z_{lin.el.}$ data of T2 topographies. Also in Fig. 4 this good agreement can be seen: Above an experimentally measured T2-topography area of $\approx 0.03\ \mu m^2$ (which relates to a mean radius of ≈ 100 nm) the measured expansion of each precipitate reaches the value determined by the linear elastic theory $\Delta z_{lin.el.} = 4.8$ nm, after Eq. (1). This value gives the maximum expected possible height, in good accordance with the experimental observation of 4.7 ± 0.5 nm.

Since the height changes Δz directly match the calculated values, we can conclude that hydrides with T2 topography cross the complete film from the film surface to the film/substrate interface. Only this assumption can explain the large out-of-plane expansion, an incomplete hydride formation would result in reduced surface topography heights. Further, because no out-of-plane stress is implemented in the calculation, we have to conclude that the precipitates expand practically freely in vertical directions. Any interface stress between the α-phase matrix and the precipitates must be, therefore, negligible for the large T2-topography-related hydrides.

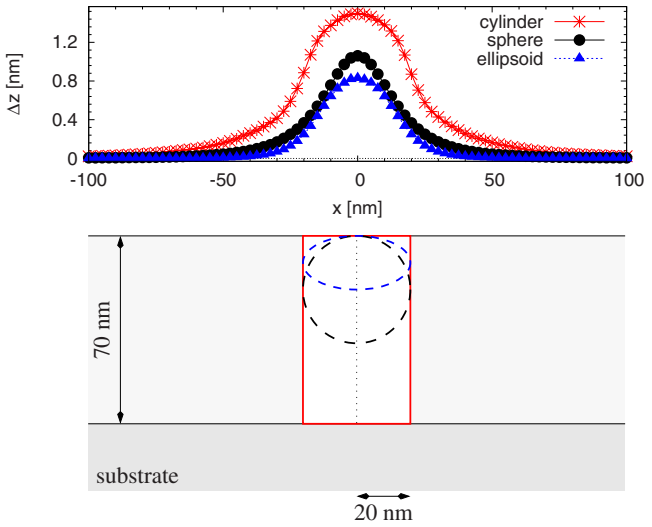

FIG. 6. (Color online) Finite element method calculations of coherent precipitates in a thin film. The lower part displays the original shape and position of the precipitates. The upper graph shows the resulting height profile of the film surface. The largest height belongs to cylindrical precipitates ranging through the complete film.

Pressure reduction does not change the surface T2 topographies. This irreversibly suggests an irreversibility of the related microstructure during hydride formation. This differs from the case of yttrium-hydride where a reversible transformation was found.[20,44,45]

T1 topographies evolve completely differently: They always show a reduced height compared to the T2 topographies and their surface roughness is similar to that of the virgin film surface. At reduced pressures T1 topographies were not detected. Even though it cannot yet be concluded that T1 topographies evolve and dissolve reversibly, it is very likely. Further measurements have to be done to confirm this point.

The absence of glide steps on the T1 topographies demonstrates the absence of dislocations formation for the T1 topographies. Further, the border between the α-phase-related surface and the T1 topographies is smooth. This is a strong hint for a lattice matching between the T1-topography-related hydrides and the original film is perfect, meaning that T1-related hydrides are coherent to the matrix.

To understand the origin of T1 topographies, finite element method calculations were performed on hydride precipitates with different shape and position in the Nb film. For these calculations the COMSOL MULTIPHYSICS[46] program package was used.

As a model, three-dimensional films of different film thicknesses were fixed to a thick and rigid substrate. Elastic properties of niobium and sapphire were implemented. For simplicity, the films were assumed to behave isotropically. Film expansion was not allowed over the substrate borders in lateral x and y directions. This accounts for the film clamping condition. Precipitates of different shapes, sizes and positions were included in the films, as shown in Fig. 6. The elastic properties of Nb were also used for the precipitates, since data for niobium hydride are missing. The hydrogen-related lattice expansion was implemented by setting an initial strain of $\epsilon=2.9\%$ in all three directions. This value contains the bulk Nb-H expansion of $0.058c_H$ and the thin films miscibility gap, $\Delta c_H=0.5$ H/Nb. Sliding between precipitates and the film was not allowed. These calculations, therefore, only deal with coherent precipitates. Shape, size and positions of the precipitates were modified and the resulting surface topography (height increase Δz) as well as the strain- and stress-fields were analyzed. This was performed for films with different thicknesses.

The height increase Δz at the surface of a 70 nm film is plotted in Fig. 6 which results for cylindrical, spherical and ellipsoidal precipitates. All precipitates are located right below the original film surface. The focus was set on shapes with circular surface topography because T1 topographies appear approximately circular. For precipitates with constant lateral diameters (radius $r_{\text{prec.}}=20$ nm) but different shapes the surface topographies differ strongly. The largest surface height change, as expected, stems from the cylindrical precipitate. All other precipitate shapes (sphere and ellipsoid) in Fig. 6 result in smaller height changes Δz, even when positioned right at the film surface. The lateral extension of the surface topography exceeds that of the precipitate causing this topography change. When the precipitates are located in the film below the surface, the Δz decreases while the lateral extension of the hillock at the surface increases in x and y directions.

For a 20 nm cylindrical precipitate in a 70 nm film the determined maximum height change is $\Delta z=1.4$ nm. Surprisingly, for smaller cylindrical precipitates the maximum height is nearly independent of film thickness. This shows the strong influence of the vertical clamping between the precipitate and the film matrix. This effect was also observed in the experiment where no film thickness dependency was found for the height data Δz of T1 topographies, as can be seen in Fig. 5.

The surface topography resulting from FEM calculations nicely matches the line profile of T1 topographies. This is exemplarily shown in Fig. 2 where a result of a calculation on a 27 nm cylindrical hydride precipitate in a 70 nm film is implemented. Both border profile and maximum height Δz are in good agreement. Surface topographies obtained by ellipsoidal or spherical precipitates do not match the experimental data, neither by the border profile nor by the height.

To compare lateral surface topography extensions of the FEM calculation, resulting from precipitates of certain radius $r_{\text{prec.}}$, with the experimentally obtained results, a surface topography radius r has to be extracted. For large precipitates the radius r was determined by a cut-off minimum height value of $\Delta z_{\text{cut.}}=0.5$ nm. For precipitates with extensions smaller than $r_{\text{prec.}}=15$ nm this cut-off value was continuously decreased to $\Delta z_{\text{cut.}}=0.2$ nm. This procedure was used for the topography data of the calculation and the experiments.

The derived height Δz and size r data obtained by FEM calculations on precipitates with different shapes in a 70 nm film are implemented in Fig. 4. Those data gained with cylindrical precipitate shape (— ·) match the experimentally observed heights. Again, heights derived from spherical or ellipsoidal precipitates Δz are too small.

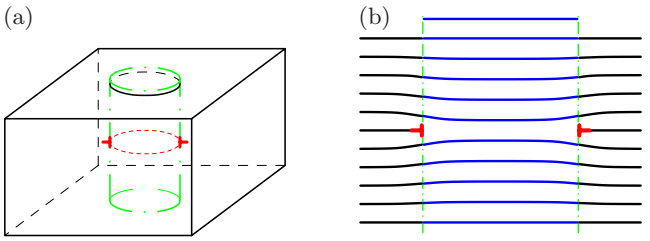

FIG. 7. (Color online) (a) Sketch of *s* dislocation loop accounting for the mismatch between a cylindrical precipitate and the matrix. (b) Two-dimensional sketch of the lattice planes and the dislocation loop. In this sketch the different lattice parameter of the precipitate with a_H and the surrounding matrix with a_α is 10% and, thus, the first and 11th plane are not bent. The implementation of the loop leads to one additional plane at the surface.

The observed agreements between the calculation and the experiments suggest a proper description of the system by the border conditions used in the FEM calculation. Further, the results give evidence for cylindrical precipitates that range from the film/substrate interface to the film surface, even for small precipitate sizes. This is in good accordance with high-resolution electron microscopy results on Nb/Pd multilayers reported by Borchers *et al.*[47]

Comparison of the experimental data with the calculated height changes suggests three different regimes visible in Fig. 4: For small sizes ($\mathcal{A}$) T1 topographies ("hillocks") are visible, for large sizes ($\mathcal{C}$) large T2 topographies are visible, and in between a transition regime ($\mathcal{B}$) consisting of T2-like topographies of smaller height Δz than the maximum height are shown. In ($\mathcal{A}$), the out-of plane expansions of the small T1 topographies correspond to the data of cylindrical precipitates vertically clamped in the thin film, as calculated by FEM. These precipitates can be regarded as coherent to the matrix, thus causing significant interface stress.

Up to a radius of $r_{crit}=36\pm3$ nm only T1 precipitates are present, as derived from the related topographies in STM images. Precipitates above this size show surface topographies with increased height and with higher surface roughness, T2-like topographies. But, they don't show the large vertical height, as found for the large T2 precipitates—they show an intermediate height. Surface roughening (which relates to dislocation formation, see Sec. II C) as well as the increase in lateral height leads to the assumption that in this region $\mathcal{B}$ the coherent matching to the α-phase matrix is destroyed by implementing dislocations. This is also in accordance with the FEM calculations which match the experimental data only up to the radius of $r_{crit}=36\pm3$ nm (see Fig. 4). The matching between the FEM calculation results and the experimental data requires lattice coherency. Deviations are expected above r_{crit} which should be similar to that size, where the first dislocation can be implemented. It is reasonable to assume that the transition should occur when the elastic energy stored in the precipitate exceeds the self-energy of one dislocation loop located around the cylindrical precipitate as shown in Fig. 7. To verify this interpretation, the film thickness dependency of the critical size for transition, r_{crit} in Fig. 5(a), should also result from the energy balance between the elastic energy and the dislocation loop self-energy.

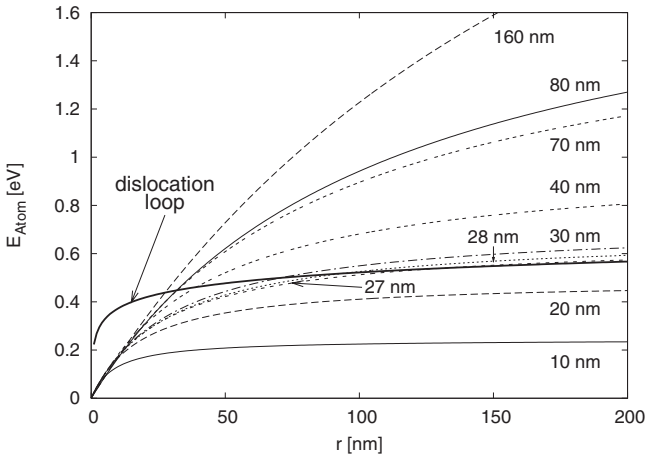

FIG. 8. Elastic energy of coherent cylindrical precipitates in films of different thicknesses d_0 (indicated at each curve). The elastic energy is normalized to the number of interface atoms between precipitate and film. First, E_{Atom} increases with the precipitate size and, finally, it saturates. The saturation value is reached at a precipitate size of $r\approx10\times d_0$ leading to a value of $E_{Atom,\infty}\approx d_0\times0.024$, where d_0 is given in nm. Also implemented is the calculated self-energy of one dislocation loop. This curve crosses the elastic energy curves for all films with a thickness above 26.3 nm. The crossover precipitate radius r_{crit} depends on the film thickness.

The elastic strain energy of a coherent cylindrical precipitate is derived from the FEM calculations for different precipitate sizes and film thicknesses. In Fig. 8 the energies per interface atom are plotted for the different film thicknesses (10 nm–160 nm). With the used normalization, the energy per atom saturates at a value which is proportional to the film thickness. The saturation is reached approximately at a radius of $r\approx10\times d_0$. The normalization was done because the deformation field in such a precipitate is focused to the interface. In Fig. 8, the self-energy of a dislocation loop is plotted too. The self-energy is calculated by adjusting the formula of Kroupa who calculated the deformation energy of a circular intrinsic dislocation loop in an unlimited isotropic medium:[8]

$$E_{Atom}(r)=\frac{Mb^2\zeta}{2(1-\nu)}\left(\ln\frac{8r}{\varrho}-1\right), \tag{2}$$

where M is the Young's modulus of niobium (105 GPa), b is the Burgers vector ($b=0.286$ nm), and ν is the Poisson ratio (0.387).[48] ϱ is the cut-off radius for the dislocation core. In the present work, this was set to one third of the Burgers vector as proposed by Suzuki *et al.*[49] The constant $\zeta=r/2\pi rh$ includes the height h of the deformation field and accounts for the normalization to the total number of interface atoms. The description of Kroupa[8] shows a fast decrease in the deformation with increasing distance to the dislocation loop. However, in our case the assumption of an unlimited isotropical medium is not correct since we also have to account for the precipitate phase. Due to the different lattice parameters of hydride precipitates and α-phase matrix the deformation field is modified and more restricted toward the dislocation loop. Because of the small extension of Kroupa's

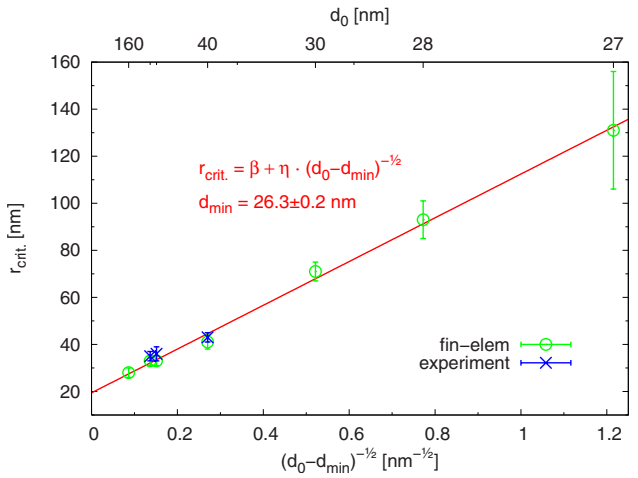

FIG. 9. (Color online) Size of precipitation r_{crit} where the elastic energy is equal to the self-energy of a dislocation loop. For precipitations larger then r_{crit} there is enough energy in the deformation field to form dislocations. Films thinner than 26.3 ± 0.2 nm cannot create dislocations and all precipitates are coherent. With increasing film thickness d_0 the transition radius r_{crit} decreases. This dependency is shown in the graph with circles. The functional dependency of these calculated values describes the experimental data for the coherent-to-semi-coherent transition which are marked with crosses.

deformation field we assume that the deformation energy can be calculated with the formula of Kroupa even for our problem. In a simplified picture, we restrict the deformation field to a cylindrical volume with the height $h=a^2/\Delta a$. At this height, both lattices match again. This is schematically shown in Fig. 7(b). Thus, the self-energy of the deformation field given by Eq. (2) is restricted to this extension. Different self-energies are calculated depending on the precipitate sizes r. Film thickness effects were neglected since all films are thicker than the deformation field extension. In Fig. 8 the calculated self-energy is given per number of interface atoms for comparison with the elastic energy of the strained precipitate. According to our model, the formation of a dislocation loop occurs when the elastic energy of the strained precipitate overcomes the dislocation loop self-energy. We note that any nucleation processes are neglected in this treatment.

Figure 8 shows that for all film thicknesses small precipitates do not contain enough elastic energy to create a dislocation loop. Here, the elastic energy curves lie below that of the dislocation loop. But, by increasing the precipitate size the elastic energy curve (which depends on the film thickness) crosses that of the dislocation loop energy. Beyond this crossover precipitate size, the presence of a dislocation loop is energetically favorable. For the 160 nm film this happens at a radius of $r_{crit}=28 \pm 2$ nm. Above this precipitate size a dislocation loop is energetically preferred. As can be seen in Fig. 8 there is a strong film thickness dependency. In thinner films larger precipitates are necessary to form a dislocation loop. This is due to the reduced elastic energy stored in precipitates in thinner films.

The film thickness dependency of the crossover precipitate size will be discussed in the following: In Fig. 9, r_{crit} is plotted depending on the film thickness d_0 in units of $1/\sqrt{d_0 - 26.3 \pm 0.2\ \text{nm}}$. The film thickness of 26.3 ± 0.2 nm gives the threshold value below which the dislocation loop self-energy curve does not cross the elastic energy curve anymore. For completeness, the accounting thickness axis is given at the top of the figure. As can be seen, the critical size of this transition increases with decreasing film thickness. Furthermore, it is shown that all data points evaluated by using finite element method for elastic energy determination and dislocation loop energies can be described by the following analytical formula:

$$r_{crit} = \beta + \eta/\sqrt{d_0 - 26.3 \pm 0.2\ \text{nm}}. \quad (3)$$

This formula links the critical precipitate size to the film thickness. Thus, critical sizes can be obtained by simply using this formula. A detailed verification of this fundamental relation that links the critical size for the coherent-to-semi-coherent transition to the film thickness for different materials is a topic of further research. Also, a deeper theoretical understanding of the rather simple dependency is not yet present.

However, Eq. (3) shows that below a film thickness of 26.3 ± 0.2 nm the creation of a dislocation loop around a precipitate is not possible. Thus, thinner films should not contain any semi-coherent or incoherent precipitates.[50] This is in good agreement with experimental observations on 20 nm films where T2 topographies were not detected.

The experimental data of the T1-T2 transition of precipitates with the radius r_{crit} (marked with crosses in Fig. 9) are nicely characterized by the functional dependency of Eq. (3). Therefore, it can be concluded that the interpretation holds and the transition between coherent T1 precipitates and semi-coherent T2 precipitates occurs at r_{crit}, which is the critical size at which one dislocation loop is formed. Above r_{crit}, FEM calculation results differ from the experimental heights. This is marked with region $\mathcal{B}$ in Fig. 4. The implementation of further dislocation loops for growing T2 precipitates leads to a height increase of the surface topography in region $\mathcal{B}$ up to the maximum value of the very large T2 precipitates, that relate to region $\mathcal{C}$. Interface stress between the precipitate and the host lattice is zero in this state. To conclude, we have three states, marked with $\mathcal{A}$, $\mathcal{B}$, and $\mathcal{C}$ in Fig. 4. In region $\mathcal{A}$, precipitates are coherent, in region $\mathcal{B}$ they are semi-coherent with concomitant nucleation of more and more dislocation loops and remaining interfacial stress between the precipitate and the matrix. In region $\mathcal{C}$ precipitates are semi-coherent with maximum dislocation number and negligible interfacial stress between the precipitate and the matrix.

IV. SUMMARY

STM-surface analyses yield strong surface topography changes upon hydride formation in thin epitaxial niobium films. Two different surface topographies were detected that differ in height and lateral extension. Whereas below a critical radius only hillock-like T1 topographies were found, at larger radii high T2 topographies were observed. Calculations by the finite element method and by the theory of linear elasticity show that both topographies belong to precipitates ranging from the film surface to the film/substrate interface.

While T1-related precipitates are mainly cylindrical in shape and coherent to the matrix, T2-related precipitates are elongated and contain dislocations: This led to the interpretation that a coherent-to-semi-coherent transition transfers T1 precipitates into T2 precipitates. This interpretation was verified by comparing the elastic energy stored in stressed coherent precipitates with that needed for dislocation loop formation. The intercept point yields the critical radius [Eq. (3)] which is, as expected, film thickness dependent. Calculation and experimental results are in good agreement. For 70 nm films a critical radius of 36 ± 3 nm was determined, for 40 nm films it increases to 40 ± 2 nm. From this interpretation it results that below a film thickness of 26 nm the transition should not occur at all. In accordance with this, T2 topographies experimentally have not been detected for 20 nm films. For the niobium-hydrogen thin film system the coherent-to-semi-coherent transition explains the experimental findings. The generality of this treatment is a further question of interest which should be tested by studying different film systems. For niobium thin films the proposed interpretation gives limits for fundamental research based on coherent precipitates in thin films which should be performed at film thicknesses below 26 nm.

ACKNOWLEDGMENTS

The authors would like to thank the Deutsche Forschungsgemeinschaft for financial support via SFB Grant No. 602 (project A9).

*apundt@ump.gwdg.de

[1] R. Becker and W. Döring, Ann. Phys. **416**, 719 (1935).
[2] M. Volmer and A. Weber, Z. Phys. Chem. **119**, 277 (1926).
[3] J. S. Langer and A. J. Schwartz, Phys. Rev. A **21**, 948 (1980).
[4] R. W. Cahn and P. Haasen, *Phase Transformations in Materials* (Wiley, Weinheim, 1991), Vol. 5.
[5] R. Kampmann and R. Wagner, *Decomposition of Alloys: The Early Stages* (Pergamon, Oxford, 1984), p. 91.
[6] M. F. Ashby, S. H. Gelles, and L. E. Tanner, Philos. Mag. **19**, 757 (1969).
[7] M. F. Ashby and L. Johnson, Philos. Mag. **20**, 1009 (1969).
[8] F. Kroupa, Czech. J. Phys., Sect. A **10**, 284 (1960).
[9] C. H. Su and P. W. Voorhees, Acta Mater. **44**, 1987 (1996).
[10] C. H. Su and P. W. Voorhees, Acta Mater. **44**, 2001 (1996).
[11] T. Al-Kassab and R. Kirchheim, Mater. Sci. Eng., A **324**, 168 (2002).
[12] K. Thornton, N. Akaiwa, and P. Voorhees, Acta Mater. **52**, 1353 (2004).
[13] K. Thornton, N. Akaiwa, and P. Voorhees, Acta Mater. **52**, 1365 (2004).
[14] R. Feenstra, D. G. de Groot, J. H. Rector, E. Salomons, and R. Griessen, J. Phys. F: Met. Phys. **16**, 1953 (1986); http://stacks.iop.org/0305-4608/16/1953
[15] H. Zabel and A. Weidinger, Comments Condens. Matter Phys. **17**, 239 (1995).
[16] A. Pundt and R. Kirchheim, Annu. Rev. Mater. Res. **36**, 555 (2006).
[17] J. Weismüller, in *Nanocrystalline Metals and Oxides: Selected Properties and Aplications*, edited by P. Knauth and J. Schoomann (Kluwer, Boston, 2001), pp. 1–39.
[18] G. Song, M. Geitz, A. Abromeit, and H. Zabel, Phys. Rev. B **54**, 14093 (1996).
[19] E. J. Grier, O. Kolosov, A. K. Petford-Long, R. C. C. Ward, M. R. Wells, and B. Hjörvarsson, J. Phys. D **33**, 894 (2000).
[20] D. G. Nagengast, J. W. J. Kerssemakers, A. T. M. van Gogh, B. Dam, and R. Griessen, Appl. Phys. Lett. **75**, 1724 (1999).
[21] J. W. J. Kerssemakers, S. J. van der Molen, N. J. Koeman, R. Günther, and R. Griessen, Nature (London) **406**, 489 (2000).
[22] A. Pundt, M. Getzlaff, M. Bode, R. Kirchheim, and R. Wiesendanger, Phys. Rev. B **61**, 9964 (2000).
[23] A. Pundt, U. Laudahn, U. v. Hülsen, U. Geyer, T. Wagner, M. Getzlaff, M. Bode, R. Wiesendanger, and R. Kirchheim, in *Thin Films—Stresses and Mechanical Properties VIII*, edited by R. Vinci *et al.*, MRS Symposia Proceedings No. 594 (Materials Research Society, Pittsburgh, 2000), p. 75.
[24] *Hydrogen in Metals I*, Topics in Applied Physics Vol. 28, edited by G. Alefeld and J. Völkl (Springer-Verlag, Berlin, 1978).
[25] B. J. Makenas and H. K. Birnbaum, Acta Metall. **28**, 979 (1980).
[26] T. Schober, Scr. Metall. **7**, 1119 (1973).
[27] Sieverts law cannot be simply applied to thin films since microstructure and mechanical stress changes the materials properties (Refs. 16 and 51).
[28] T. Schober and H. Wenzl, *Hydrogen in Metals II*, Topics in Applied Physics Vol. 29 (Springer-Verlag, Berlin, 1978), Chap. 2.
[29] J. A. Pryde and C. G. Titcomb, Trans. Faraday Soc. **65**, 2758 (1969).
[30] G. Andersson, B. Hjörvarsson, and H. Zabel, Phys. Rev. B **55**, 15905 (1997).
[31] Q. M. Yang, G. Schmitz, S. Fähler, H. U. Krebs, and R. Kirchheim, Phys. Rev. B **54**, 9131 (1996).
[32] U. Laudahn, A. Pundt, M. Bicker, U. von Hülsen, U. Geyer, T. Wagner, and R. Kirchheim, J. Alloys Compd. **293-295**, 490 (1999).
[33] K. Nörthemann, R. Kirchheim, and A. Pundt, J. Alloys Compd. **356-357**, 541 (2003).
[34] K. Yoshii, H. Yamamoto, K. Saiki, and A. Koma, Phys. Rev. B **52**, 13570 (1995).
[35] V. Oderno, C. Dupour, K. Dumesnil, A. Mougan, P. Mangin, and G. Marchal, Philos. Mag. Lett. **78**, 419 (1998).
[36] E. J. Grier, M. L. Jenkins, A. K. Petford-Long, R. C. C. Ward, and M. R. Wells, Thin Solid Films **358**, 94 (2000).
[37] A. R. Wildes, J. Meyer, and K. Theis-Bröhl, Thin Solid Films **401**, 7 (2001).
[38] J. Steiger, S. Blässer, and A. Weidinger, Phys. Rev. B **49**, 5570 (1994).
[39] G. Song, A. Remhof, K. Theis-Bröhl, and H. Zabel, Phys. Rev. Lett. **79**, 5062 (1997).
[40] C. Rehm, F. Klose, D. Nagengast, H. Maletta, and A. Weidinger, Physica B **234-236**, 486 (1997).
[41] C. Rehm, H. Fritzsche, H. Maletta, and F. Klose, Phys. Rev. B

59, 3142 (1999).
[42] A. Pundt, K. Nörthemann, and S. Schmidt, J. Alloys Compd. **446-447**, 549 (2007).
[43] M. Dornheim, Ph.D. thesis, Georg-August-Universität zu Göttingen, 2002.
[44] A. Remhof, J. W. J. Kerssemakers, S. J. v. d. Molen, R. Griessen, and E. S. Kooij, Phys. Rev. B **65**, 054110 (2002).
[45] J. W. J. Kerssemakers, S. J. van der Molen, R. Günther, B. Dam, and R. Griessen, Phys. Rev. B **65**, 075417 (2002).
[46] COMSOL MULTIPHYSICS version 3.2, www.comsol.com, with "Structural Mechanics Module."
[47] C. Borchers, U. Laudahn, A. Pundt, S. Fähler, H.-U. Krebs, and R. Kirchheim, Philos. Mag. A **80**, 543 (2000).
[48] K. H. Hellwege and O. Madelung, *Zahlenwerte und Funktionen aus Naturwissenschaften und Technik*, Landolt Börnstein, New Series, Group III, Vol. 18 (Springer-Verlag, Berlin, 1984).
[49] T. Suzuki, S. Takeuchi, and H. Yoshinaga, *Dislocation Dynamics and Plasticity*, Springer Series in Material Science Vol. 12 (Springer-Verlag, New York, 1989).
[50] The semi-coherent state is the state where the lattice between precipitate and host lattice partially match and some dislocations are implemented.
[51] S. Wagner and A. Pundt, Appl. Phys. Lett. **92**, 051914 (2008).